Real-Time SLAM-Based Correction and 3D Visualization for Fluorescence Lifetime Imaging

Murali Krishnamoorthy[1*][0000−0002−4834−4991], Haoyin Zhou[2*][0000−0002−1334−8060], Katherine Frazee[1][0009−0009−6867−8428], Rahul Pal[1][0000−0003−2586−4991], Jayender Jagadeesan[2][0000−0002−3308−3012], and Anand T.N. Kumar[1][0000−0002−8745−9599]

[1] Department of Otolaryngology – Head and Neck Surgery, Massachusetts Eye and Ear Hospital, Harvard Medical School, Boston, MA, USA
[2] Department of Radiology at Brigham and Women's Hospital Harvard Medical School, Boston, MA, USA *
Email: anand_kumar@meei.harvard.edu

Abstract. Fluorescence lifetime (FLT) imaging has been shown to distinguish tumors from normal tissue with high accuracy. However, the practical utility of FLT imaging is hindered by slow acquisition speeds and depth-dependent inaccuracies. To address these challenges, we introduce FLT-SLAM, a novel algorithm that combines rapid FLT imaging with simultaneous localization and mapping (SLAM) for real-time 3D surface reconstruction and depth-corrected FLT estimation. Using a stereo laparoscope, our approach extracts real-time depth information to improve accuracy, while achieving acquisition speeds exceeding 5 Hz. FLT maps are overlaid onto large-scale 3D surface models generated by SLAM, improving visualization and spatial awareness. We validate FLT-SLAM through phantom and ex-vivo tissue measurements, and show that it reduces FLT estimation errors by nearly 20%, thereby demonstrating its potential to enhance real-time, depth-corrected FLT imaging for surgical applications.

Keywords: Fluorescence lifetime imaging · SLAM · depth correction · intuitive visualization

1 Introduction

Accurately distinguishing healthy tissue from cancer remains a major challenge in surgery, directly impacting the completeness of tumor resection and in turn, the long term prognosis for the patient. Surgeons primarily rely on visual inspection and palpation, which are often imprecise, increasing the risk of incomplete tumor removal or unnecessary excision of healthy tissue [1]. Near-infrared (NIR) fluorescence imaging, using tumor-targeted fluorescent agents [2–5] is currently being widely explored to enhance tumor contrast during surgeries. While

Murali Krishnamoorthy and Haoyin Zhou have equal contribution to this work.

these agents offer improved performance over direct visual inspection, they often exhibit variable uptake in tumor tissue and non-specific uptake in healthy tissue. This variability compromises sensitivity and contributes to high false positive rates in tumor identification [6]. A major limitation of existing molecularly targeted agents is their reliance on fluorescence intensity measurements, which cannot differentiate between tumor-specific and non-specific uptake [7].

Recent studies have demonstrated that fluorescence lifetime (FLT) imaging can detect tumors at a microscopic level with high accuracy ($> 97\%$) in patients injected with tumor-targeted NIR contrast agents [7]. Fluorescence lifetime, a fundamental photophysical quantity [8] is obtained by measuring the decay profile of light after pulsed excitation, which typically requires multiple measurement points, making it time-consuming. A recently proposed method that combines a single time gate and fluorescence intensity measurement has been shown to enhance the speed of FLT imaging in real time [12]. However, to effectively implement this method during surgeries, it is necessary to accurately measure the depth of the tissue in real-time, in the presence of dynamic tissue deformation and structural variations. Another challenge in FLT imaging with laparoscopes is the limited field-of-view (FOV).

To address these issues, we propose a novel algorithm that integrates depth information into FLT imaging using our previously developed simultaneous localization and mapping (SLAM) algorithm [11]. SLAM enables real-time depth estimation for each pixel from stereo laparoscope images at a rate of up to 25 Hz. This approach eliminates the need for additional devices, offering a significant advantage for clinical implementation. To overcome the limited FOV, our proposed method overlays FLT imaging onto a large-scale 3D surface model constructed by the SLAM algorithm using white-light video data from a stereo laparoscope, providing a comprehensive and intuitive visualization of the surgical field. We demonstrate that our method enables accurate FLT measurements in a wide field of view (FOV) ($> 1000 \times 1000$ pixels, $> 8cm^2$ FOV) at high speeds (> 5 Hz).

Our approach integrates FLT imaging with large-scale 3D surface modeling using SLAM to enhance real-time surgical visualization. By leveraging SLAM, we extract precise depth information, which is iteratively incorporated to refine FLT estimation in real time. Through theoretical analysis and simulations, we demonstrate that this iterative method converges to the true FLT values. We further validate our approach using step-shaped phantoms and *ex vivo* tissue models, including breast, liver, and kidney tissues, highlighting its potential for use during surgeries.

2 Methods

The system consists of a custom-built wide-field time-gated intensifier (Picostar, LaVision) coupled to a CMOS camera (Basler acA5472-17um) for FLT measurements, and a white-light stereo laparoscope (0^0, 10 mm Karl Storz TipCam), used concurrently with the intensifier for image acquisition (Fig. 1a). The sam-

ple (S) is illuminated with a pulsed laser source (Toptica FFSmart, 780 nm, 80 MHz repetition rate, 150 fs pulse width) via a diffuser (D). Emission light is collected through the lens (L) and filter (F: 830 ± 30 nm), and the time domain (TD) fluorescence images are acquired with integration times between 0.1 and 1 second. A second CMOS camera to directly measure fluorescence intensity, positioned after the emission filter and coupled via a 50:50 beam splitter (Thorlabs CCM1-BS014), records continuous-wave (CW) images. Gated imaging is performed with a 600 V gain, 600 ps gate width, and 20-200 ps time steps for conventional TD, capturing a total signal duration of 6 ns.

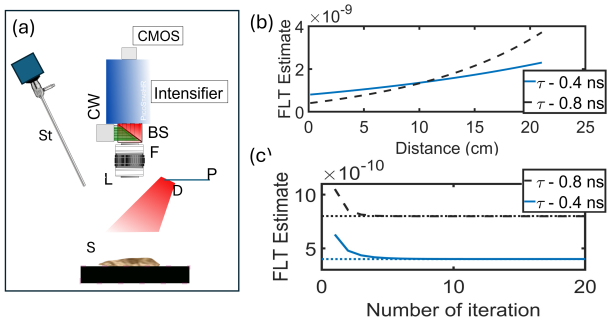

Fig. 1. (a) Schematic of the imaging system that concurrently uses a widefield FLT system and a stereo laparoscope (ST). The widefield FLT system comprises an intensifier to obtain the single-gate measurement and a CW camera to measure fluorescence intensity. The sample (S) is illuminated by a pulsed laser source (P) through a diffuser (D). The emission light is captured using a lens (L) and an emission filter (F) (830 ± 30 nm), and a beam splitter (50:50) splits the light between the gated intensifier and the CW camera. (b) FLT estimation using the Fast FLT method (without depth correction) shows an incorrect estimate of FLT. Here, τ values of 0.4 ns and 0.8 ns are shown (solid and dashed lines, respectively). (c) The proposed iterative method accurately recovers the true FLT values—0.8 ns at 5 cm depth (black dotted line) and 0.4 ns at 3 cm depth (blue dotted line), within approximately 5 iterations.

Theory: The signal from the gated intensifier is modeled as an integral of the fluorescent exponential decay as,

$$I_1(r,T) = \int_{t(r)}^{t(r)+T} a(r)e^{-t'/\tau(r)}dt' = I_{CW}(r)e^{-t(r)/\tau(r)}\left(1-e^{-T/\tau(r)}\right), \quad (1)$$

where r represents the 2-D spatial location on the sample, T is the gate width, $t(r)$ is the time offset corresponding to the start of the gate and depends on the distance of the sample from the camera at location r, $I_{CW} = \int_0^\infty ae^{-t/\tau}dt = a\tau$ is the continuous wave (CW) fluorescence intensity, and τ is the fluorescence lifetime. For simplicity, we drop the spatial coordinate r henceforth. The inverse

problem involves determining the lifetime τ, which is obtained from Eq. (1) as:

$$\tau = -\frac{T}{\ln\left(1 - \frac{I_1 e^{-t/\tau}}{I_{CW}}\right)}. \tag{2}$$

Equation (2) is non-linear in τ due to the presence of the term $e^{-t/\tau}$ on the right-hand side. To solve it, we employ an iterative approach using the following linearized method:

1. Assume $e^{-t/\tau} \approx 1$, and solve for τ (across all locations r) in the first iteration (denoted as τ_1).
2. Use this computed value, τ_1, in the second iteration, updating the term e^{-t/τ_1} and solving for a refined value, τ_2.
3. Repeat this process iteratively, defining τ_n such that it converges to the true value τ^*.

Convergence Analysis: The objective of the convergence analysis is to establish that the iterative sequence τ_n converges to the true lifetime τ^* under reasonable conditions. To solve this, we define the iterative approach as:

$$\tau_{n+1} = F(\tau_n) = -\frac{T}{\ln\left(1 - \frac{I_1 e^{-t/\tau_n}}{I_{CW}}\right)}. \tag{3}$$

To demonstrate convergence, we must show the following: (a) the sequence satisfies contraction mapping conditions [13] and (b) it is bounded and monotonic in nature.

Contraction Mapping Condition: The iterative function $F(\tau)$ satisfies the contraction mapping condition if there exists a constant $0 \leq c < 1$ such that:

$$|F'(\tau)| \leq c < 1, \quad \forall \tau > 0. \tag{4}$$

Differentiating $F(\tau)$, we get:

$$F'(\tau) = -\frac{I_1 T t \mathrm{e}^{-\frac{t}{\tau}}}{I_{CW}\tau^2\left(1 - \frac{I_1 \mathrm{e}^{-\frac{t}{\tau}}}{I_{CW}}\right)\ln^2\left(1 - \frac{I_1 \mathrm{e}^{-\frac{t}{\tau}}}{I_{CW}}\right)}.$$

For typical τ values ranging between 0.5–2 ns and sample depth variation less than 5 cm (which determines the range of t/τ), we numerically ensured hat $|F'(\tau)| < 1$. By the Banach Fixed-Point Theorem [13], this guarantees unique convergence to actual FLT τ^*.

Boundedness: To prove that the iterative sequence τ_n remains bounded, we show the existence of finite constants $\tau_{\min}$ and $\tau_{\max}$ such that:

$$0 < \tau_{\min} \leq \tau_n \leq \tau_{\max} < \infty, \quad \forall n. \tag{5}$$

Lower Bound: From the iteration formula in equation (3), we can see that

$1 - \frac{I_1 e^{-t/\tau_n}}{I_{CW}} > 0$ for $t > 0$, since $I_1 < I_{CW}$, ensuring that τ_n remains positive. Hence, there exists a finite lower bound $\tau_{\min} > 0$.
Upper Bound: As $\tau_n \to \infty$, we have $e^{-t/\tau_n} \to 1$, implying: $1 - \frac{I_1 e^{-t/\tau_n}}{I_{CW}} \to 1 - \frac{I_1}{I_{CW}}$. The logarithmic term remains finite, and hence, τ_n is bounded above by a finite $\tau_{\max}$.

Monotonicity: If τ_n is always increasing or decreasing, it avoids oscillations and settles at τ^*. Using $\tau_{n+1} - \tau_n = F(\tau_n) - \tau_n$, and noting that e^{-t/τ_n} is always less than 1 for all $t > 0$ and $\tau_n > 0$, we can apply the Monotone Convergence Theorem [14]. Since, τ_n is monotonic and bounded, it must converge to τ^*.
Simulations: We demonstrate numerically that the iterative function described above converges reliably. To illustrate this, we simulated the gated intensity I_1 and fluorescence intensity I_{CW} for two fluorescence lifetimes: 0.8 ns and 0.4 ns. The corresponding gated intensities were generated using depths of 5 cm and 3 cm, respectively. Starting with an initial estimate that neglects depth delay, we applied the iterative correction method to update the fluorescence lifetime estimate. As shown in Fig. 1(c), the sequence converges to the true lifetime value within approximately five iterations. We have verified similar convergence behavior across a range of lifetimes and depths.
SLAM-Based Depth Estimation for FLT Imaging: In real clinical settings, tissue depth relative to the camera varies, introducing uncertainties in estimating τ. To address this, we integrate the SLAM algorithm with FLT imaging to obtain precise depth measurements and compensate for inaccuracies in τ estimation. Further, the FLT imaging is overlaid onto the 3D reconstructed models generated using SLAM to provide an intuitive visualization of the combined white-light and FLT images.

We leveraged our previously developed SLAM algorithm to generate high-resolution, dense 3D models of tissue surfaces from stereo laparoscopy images. The algorithm begins by performing GPU-accelerated stereo matching between left and right laparoscopic images, extracting pixel-level depth information in parallel. Post-processing steps, including outlier removal and smoothing, further refine depth accuracy. The resulting 2.5D depth maps are then mosaicked over time to construct large-scale 3D models in real time.

Using the calibrated transformation between the FLT camera and the laparoscope, we reproject the SLAM-based 3D model onto FLT imaging to precisely determine the depth between the FLT camera and the tissue surface. A median filter is applied in post-processing to fill gaps and enhance depth estimation. To further improve FLT imaging accuracy, we developed a novel imaging algorithm, described below, that integrates this depth data, enabling more precise and reliable fluorescence lifetime τ estimation.

To provide intuitive surgical guidance, we overlay FLT imaging onto the 3D SLAM model. Since FLT imaging can vary with changes in viewing angles, the SLAM algorithm aligns FLT images across different frames. This alignment enables the merging of FLT images by combining the maximum signal from overlapping regions, ensuring more consistent and accurate visualization.

Depth-corrected FLT: The continuous-wave (CW) camera is co-registered with the gated intensifier using Speeded-Up Robust Features (SURF) in MATLAB. The pixel-wise scaling of the CW camera is performed using white-light illumination to obtain a scaling factor (α), ensuring independence from variations in quantum yield and hot pixels between the cameras. FLT is then estimated using Equation (6), where the delay factor (t) due to depth variation is obtained from the stereo laparoscope via the SLAM algorithm. The stereo laparoscope is co-registered to the field using fiducials. The depth information (d) is converted into time delay using the speed of light in air, scaled by a factor β, that depends on the laparoscope's focal length. Thus, the final equation for lifetime estimation is given by:

$$\tau = \frac{-T}{\log\left(1 - \frac{I_1 e^{-\beta d/\tau}}{\alpha I_{CW}}\right)}. \tag{6}$$

3 Results

Phantom study For the phantom study, we designed a step-like phantom with dimensions 50.8 mm (height) × 31.75 mm (width) × 79.35 mm (length) consisting of five steps, as shown in Fig. 2(a). Small paper strips, dipped in a solution of ICG mixed with EtOH and DMSO (dimethyl sulfoxide), were used as fluorescent targets. Standard FLT imaging with 30+ time points yielded an average lifetime of 0.8 ± 0.05 ns (Fig. 2(d)), obtained by fitting each pixel to a mono-exponential model using a non-linear least squares minimization algorithm (Fig. 2(c)).

A time delay (t) of $\sim$ 255 ps was observed between the top and bottom steps (Fig. 2(d)), leading to an FLT estimation error of $\sim$ 30% (Fig. 2(d,e)). By calculating depth (d) using the stereo camera and incorporating it into Equation (6), the FLT estimation improved (Fig. 2(f,g)), reducing the mean error to $\sim$ 10%, as shown in Fig. 2(h).

Ex-vivo organs To validate the integration of SLAM-based 3D surface reconstruction with FLT imaging, images were acquired using the stereo laparoscope. A turkey breast tissue was placed on top of a curved liquid phantom (Intralipid and Indian Ink) to mimic the optical properties of the tissue, with absorption and reduced scattering coefficients of $\mu_a = 0.1$ cm^{-1} and $\mu_s' = 10$ cm^{-1}, respectively [15].

The SLAM algorithm utilized stereo vision to extract depth information, converting 2D images into detailed 3D point clouds. To address the limited field of view, multiple images were merged based on overlapping regions, generating a cohesive 3D model. Fiducial markers were used for co-registration of FLT data with stereo imaging via 6-DoF pose estimation using the P3P algorithm [16]. By overlaying positive regions from intensity and FLT images onto the reconstructed 3D surface (Fig. 3e, Fig. 3f), an intuitive visualization of the large-scale 3D model was achieved.

For FLT imaging, we used two dyes composed of ICG in DMSO and methanol, with lifetimes of 1.01 ns and 0.52 ns, respectively, mimicking the contrast between tumor and normal tissue. These dyes were placed in 100 μl – 1 ml tubes

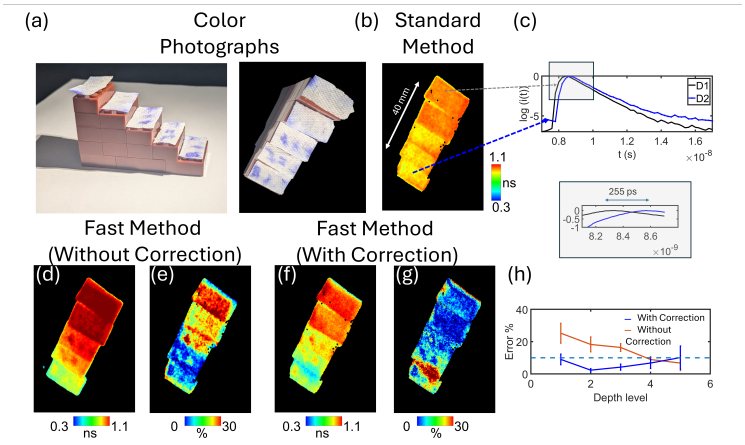

Fig. 2. Validation of the proposed approach in step-phantom (a) Color photograph of the step phantom. (b) The standard (slow, time taken 40 s) approach for FLT estimation using more than 30 time gates serves as the ground truth. (c) Time-domain (TD) data between points at a depth of 40 mm apart shows approximately a 255 ps delay in the peak of the temporal point spread function. (d) The fast approach (5 Hz) using a single gate estimates FLT with a large error compared to (b). (e) Errors in FLT estimation without depth correction. (f) Fast approach with depth correction (4.9 Hz), (g) Error map of the proposed approach with depth correction. (h) The mean error in each step shows that with the proposed approach, the mean error is less than 11%. The dotted line represents a 10% error threshold.

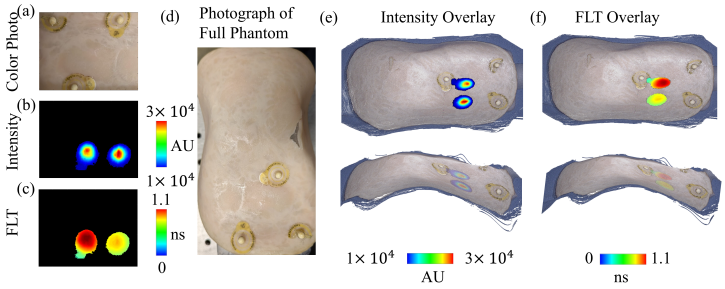

Fig. 3. (a) Color photograph of the phantom taken at small fields of view (FOV). Corresponding fluorescence intensity (b) and lifetime (c) maps highlight distinct dye characteristics. (d) A photograph of the full view of the phantom. (e) Real-time 3D overlay of the fluorescence intensity map with the reconstructed SLAM surface, and (f) overlay of the fluorescence lifetime (FLT) map with the reconstructed SLAM surface, shown in two different orientations.

and positioned beneath the tissue. Similarly, freshly resected porcine liver (18-20 cm) and kidney (10 cm) tissues were used, with vials containing the fluorophores placed approximately 1–2 mm under the tissues for FLT measurement. Depth maps were obtained in real time and later processed to generate FLT maps (Fig. 4c). For all FLT calculations, intensity was thresholded to 80% of its maximum value. In addition to the FLT overlay, we also present fluorescence intensity overlays (Fig. 4b), which do not clearly distinguish between tumor and normal tissue. To assess the impact of tissue height variation, additional experiments were performed by moving the tissue in the vertical direction by 3 cm. This resulted in an apparent lifetime shift from the expected 1.01 ns to 1.34 ns. However, after correcting for depth variations using stereo laparoscopic imaging, the estimated lifetime improved to 1.08 ns, demonstrating the importance of depth correction in FLT quantifications.

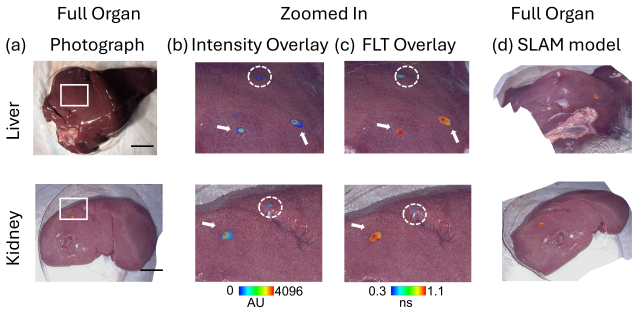

Fig. 4. Demonstration of FLT-SLAM using ex-vivo organ tissues: (a) Color photographs of porcine liver and kidney. The SLAM algorithm was used to generate the 3D surface map. Zoomed-in intensity (b) and FLT (c) images overlaid on the 3D surface are shown along with the FLT image overlaid on the full organ 3D surface map generated by SLAM (d). Long lifetimes are shown by solid arrows and short lifetimes are shown by dotted circles. Scale: 1 cm (liver) 2 cm (kidney).

4 Discussion

The FLT-SLAM algorithm improves FLT imaging in several ways: (1) incorporating depth correction for accurate FLT recovery in fast algorithms (speed $> 5Hz$), (2) overlaying FLT images on large mosaics for more intuitive navigation over wide fields of view, and (3) potentially improving FLT detection by integrating multiple FLT video frames. Future work will explore non-rigid and dynamic SLAM techniques for improved depth estimation and FLT map overlay.

In the present work, we employed FLT acquisition and white-light imaging concurrently using two different systems. Future implementations will integrate

both systems by adapting a custom-built NIR laparoscope with a stereo white-light imaging system. However, the proposed approach remains highly translatable, since we demonstrated its feasibility using a commercially available clinical laparoscope.

Another potential limitation of the SLAM-FLT approach is the influence of background light leakage on the SLAM-FLT depth estimation. While this should not be a significant issue for NIR wavelengths, the white light used to illuminate the sample for the depth camera often contains some NIR light, which can contaminate the measured fluorescence. This spurious background fluorescence can be subtracted by performing baseline measurements without the pulsed laser excitation, and by thresholding based on the total intensity. Using an additional excitation filter to block the NIR portion of the white light could further enhance imaging performance. Additionally, further studies are required to validate the impact of motion artifacts. The FLT imaging frame rate of ~ 5 Hz can be improved by using detectors with higher quantum efficiency and pulsed sources with increased illumination power. Nonetheless, this work serves as a proof-of-concept for the integration of FLT imaging with SLAM algorithms.

Acknowledgments. This study was funded by National Institutes of Health (R01-EB036978, R01-DE033427, and R01-CA260857).

Disclosure of Interests. The authors have no competing interests to declare that are relevant to the content of this article.

References

1. J. S. D. Mieog et al., "Fundamentals and developments in fluorescence-guided cancer surgery," *Nature Reviews Clinical Oncology*, vol. 19, no. 1, pp. 9–22, 2022. doi: 10.1038/s41571-021-00560-0.
2. Lauwerends, L. J., et al. (2021). Real-time fluorescence imaging in intraoperative decision making for cancer surgery. *The Lancet Oncology*, *22*(4), e186–e195.
3. Hoogstins, C. E. S., et al. (2016). A novel tumor-specific agent for intraoperative near-infrared fluorescence imaging: a translational study in healthy volunteers and patients with ovarian cancer. *Clinical Cancer Research*, *22*(12), 2929–2938.
4. Azari, F., et al. (2021). Intraoperative molecular imaging clinical trials: a review of 2020 conference proceedings. *Journal of Biomedical Optics*, *26*(5), 050901.
5. W. Stummer, et al., "Fluorescence-guided surgery with 5-aminolevulinic acid for resection of malignant glioma: a randomised controlled multicentre phase III trial," *The Lancet Oncology*, vol. 7, no. 5, pp. 392–401, 2006. doi: 10.1016/S1470-2045(06)70665-9.
6. Pogue, B. W., Rosenthal, E. L., Achilefu, S., & Van Dam, G. M. (2018). Perspective review of what is needed for molecular-specific fluorescence-guided surgery. *Journal of Biomedical Optics*, *23*(10), 100601.
7. R. Pal et al., "Fluorescence lifetime of injected indocyanine green as a universal marker of solid tumors in patients," *Nature Biomedical Engineering*, 2023. doi: 10.1038/s41551-023-01105-2.
8. Lakowicz, J. R. (1999). *Principles of Fluorescence Spectroscopy* (2nd ed.). Springer.

9. Pal, R., et al. (2022). Comparison of fluorescence lifetime and multispectral imaging for quantitative multiplexing in biological tissue. *Biomedical Optics Express*, *13*(9), 3854–3868.
10. C. Cadena et al., "Past, present, and future of simultaneous localization and mapping: Toward the robust-perception age," *IEEE Transactions on Robotics*, vol. 32, no. 6, pp. 1309–1332, 2016. doi: 10.1109/TRO.2016.2624754.
11. Zhou H., and Jayender J. : Real-time dense reconstruction of tissue surface from stereo optical video. IEEE Transactions on Medical Imaging, 39.2 (2019): 400-412.
12. M. Krishnamoorthy et al., "High-Speed Wide-Field Fluorescence Lifetime Imaging for Intraoperative Tumour Visualisation and In Vivo Multiplexing" *Research Square*, *https://doi.org/10.21203/rs.3.rs-6579067/v1*.
13. Rudin, W. (1974). *Real and Complex Analysis*. McGraw-Hill Book Co.
14. Schechter, E. (1996). *Handbook of Analysis and its Foundations*. Academic Press.
15. Kumar, A. T. N., et al. (2008). A time domain fluorescence tomography system for small animal imaging. *IEEE Transactions on Medical Imaging*, *27*(9), 1152–1163.
16. V. Lepetit et al., "EPnP: An accurate O(n) solution to the PnP problem," *International Journal of Computer Vision*, vol. 81, pp. 155–166, 2009. doi: 10.1007/s11263-008-0152-6.